Journal of
Applied
Crystallography

ISSN 0021-8898

Received 13 January 2013
Accepted 22 July 2013

Rietveld refinement, morphology and optical properties of $(Ba_{1-x}Sr_x)MoO_4$ crystals

I. C. Nogueira,[a] L. S. Cavalcante,[b,c]* P. F. S. Pereira,[a] M. M. de Jesus,[d] J. M. Rivas Mercury,[d] N. C. Batista,[c] M. Siu Li[d] and E. Longo[b]

[a]LIEC, UFSCar-DEMA, PO Box 676, 13565-905, São Carlos, SP, Brazil, [b]Instituto de Química-UNESP, PO Box 355, 14801-907, Araraquara, SP, Brazil, [c]UESPI, CCN, Departamento de Química, Rua João Cabral, PO Box 2231, 64002-150, Teresina, PI, Brazil, and [d]Instituto Federal do Maranhão, Química, CEP 65025-001, São Luís, MA, Brazil. Correspondence e-mail: laeciosc@bol.com.br

In this article, the structural refinement, morphology and optical properties of barium strontium molybdate [$(Ba_{1-x}Sr_x)MoO_4$ with x = 0, 0.25, 0.50, 0.75 and 1] crystals, synthesized by the co-precipitation (drop-by-drop) method, are reported. The crystals obtained were structurally characterized by X-ray diffraction (XRD), Rietveld refinement, and Fourier transform–Raman (FT–Raman) and Fourier transform–infrared (FT–IR) spectroscopies. The shapes of the crystals were observed by means of field-emission scanning electron microscopy (FE-SEM). The optical properties were investigated using ultraviolet–visible (UV–Vis) absorption spectroscopy and photoluminescence (PL) measurements. XRD patterns, Rietveld refinement, and FT–Raman and FT–IR spectra showed that all of the crystals are monophasic with a scheelite-type tetragonal structure. The refined lattice parameters and atomic positions were employed to model the $[BaO_8]$, $[SrO_8]$ and $[MoO_4]$ clusters in the tetragonal lattices. The FE-SEM images indicate that increased x content produces a decrease in the crystal size and modifications in the crystal shape. UV–Vis spectra indicated a decrease in the optical band gap with an increase in x in the $(Ba_{1-x}Sr_x)MoO_4$ crystals. Finally, a decrease in the intensity of PL emission is apparent with an increase in x up to 0.75 in the $(Ba_{1-x}Sr_x)MoO_4$ crystal lattice when excited by a wavelength of 350 nm, probably associated with the degree of structural order–disorder.

1. Introduction

In recent years, there has been a growing interest in the optical properties of scheelite-type molybdates with potential for use in applications such as sensors, modulators, monitors, waveguides, X-ray detectors and light-emitting diodes (Lei & Yan, 2008; Phuruangrat *et al.*, 2009; Ryu *et al.*, 2008; Spassky *et al.*, 2004; Yakovyna *et al.*, 2008). Among the inorganic materials, molybdates with scheelite-type tetragonal structures have been highlighted owing to their high photoluminescence (PL) emission at room temperature and good chemical stability (Afanasiev, 2007; Cui *et al.*, 2007; Ma *et al.*, 2010). These molybdates have a general formula ($AMoO_4$), where A is a bivalent cation (Ca^{2+}, Sr^{2+}, Ba^{2+} or Pb^{2+}) which is coordinated to eight oxygen atoms and the Mo atoms are coordinated to four oxygen atoms which belong to the tetragonal crystal system with space group $I4_1/a$ and symmetry C_{4h}^6 (Panchal *et al.*, 2006; Guo *et al.*, 2009; Sczancoski *et al.*, 2009; Yang *et al.*, 2009).

In particular, barium molybdate ($BaMoO_4$) and strontium molybdate ($SrMoO_4$) have been extensively researched owing to their PL emission in the visible spectral region (Bi *et al.*, 2008; Lei *et al.*, 2010; Liu *et al.*, 2007; Yin *et al.*, 2010). In addition, several methods have been explored to synthesize these molybdates, including a solid-state reaction (Al-Hajji *et al.*, 2003; Pupp *et al.*, 1969), a spontaneous crystallization (Spassky *et al.*, 2004), a complex polymerization (Marques *et al.*, 2005, 2008), an electrochemical method (Bi *et al.*, 2003; Sun *et al.*, 2011*a*; Xia & Fuenzalida, 2003), a microwave–hydrothermal system (Cavalcante *et al.*, 2009; Sczancoski *et al.*, 2008, 2010) and a microwave–solvothermal system (Thongtem *et al.*, 2010). Wu *et al.* (2007) obtained $BaMoO_4$ microcrystals *via* an aqueous solution mineralization process. They found that the pH and temperature of the reaction had important influences on the formation and control of the $BaMoO_4$ microcrystal shape. Shuttle-like microcrystals were obtained in an alkaline aqueous solution (pH = 9–14); when the pH value was adjusted to between 6 and 7, cocoon-like microcrystals were obtained. Cavalcante *et al.* (2008) synthesized octahedron-like $BaMoO_4$ microcrystals with intense green PL emission by a microwave–hydrothermal method at 413 K for 1 h. In another research report, Zhang *et al.* (2006) synthesized $BaMoO_4$ nanostructured by a solvothermal method which resulted in

different shapes (spindle arrays, bundle-like and brush-like). These nanostructure shapes were easily obtained by changing the temperature and the ratio of water to surfactant. Thongtem *et al.* (2010) synthesized $SrMoO_4$ nanocrystals with an average particle size of 14–40 nm using a microwave-irradiation method with ethylene glycol solvent. According to the literature (Marques *et al.*, 2010), the particle size distribution and crystallographic orientation (in the case of mesocrystals and nanocrystals with a narrow form) strongly influence the PL properties. Parameter adjustments, such as stirring time, reaction temperature, reaction time, surfactant and solvent, can modify the shape and average size of the crystals, which affect their physical and chemical properties (Cavalcante, Batista *et al.*, 2012).

Some literature reports show the influence of the replacement of the lattice modifiers by other alkaline earth metal ions on the structural properties of scheelite crystals (Porto *et al.*, 2005; Pôrto *et al.*, 2008; Rangappa *et al.*, 2008; Sun *et al.*, 2011*b*; Zhang *et al.*, 2008). Regarding the barium strontium molybdate [$(Ba_{1-x}Sr_x)MoO_4$] system, Yoshimura *et al.* (1997) obtained a $(Ba_{1-x}Sr_x)MoO_4$ thin film by the electrochemical method with a green PL emission at a cryogenic temperature. Sahu *et al.* (2012) synthesized $(Ba_{1-x}Sr_x)MoO_4$ solid solutions by a complex polymerization method and investigated their thermo-physical properties.

In this work, for the first time, the synthesis of $(Ba_{1-x}Sr_x)MoO_4$ crystals (x = 0, 0.25, 0.50, 0.75 and 1) by the co-precipitation (drop-by-drop) method is reported. Moreover, we seek to gain an understanding of how controlled variations of the chemical composition of these scheelite materials may influence their structural, morphological and optical properties.

2. Experimental details

2.1. Synthesis of $(Ba_{1-x}Sr_x)MoO_4$ crystals

$(Ba_{1-x}Sr_x)MoO_4$ crystals (x = 0, 0.25, 0.50, 0.75 and 1) were synthesized by the co-precipitation (drop-by-drop) method at 343 K. The typical experimental procedure is described as follows: 0.001 mol of sodium molybdate dihydrate ($Na_2MoO_4\cdot 2H_2O$) (99.5% purity, Sigma–Aldrich), 0.001 mol of barium nitrate [$Ba(NO_3)_2$] (99% purity, Sigma–Aldrich) and 0.001 mol of strontium nitrate [$Sr(NO_3)_2$] (99.5% purity, Sigma–Aldrich) salts were employed as the starting precursors. In this co-precipitation method, 50 ml of an aqueous solution of Ba^{2+} and Sr^{2+} ions was slowly dripped, at a flow rate of 10 ml min^{-1}, into 50 ml of an aqueous solution containing MoO_4^{2-} ions (at 343 K) held in a 250 ml Erlenmeyer flask. The drip was performed with the aid of a Masterflex 77240-10 L/S compact variable-speed pump. For all systems, the temperature was kept at 343 K for 30 min, pH = 7, and the agitation rate in an IKA C-MAG HS-7 magnetic stirrer was 700 r min^{-1}. In general, the precipitation reaction occurs because Ba^{2+}/Sr^{2+} cations are electron-pair acceptors (Lewis acids) while MoO_4^{2-} anions are electron-pair donors (Lewis bases). The reactions between these two species ($Ba^{2+}/Sr^{2+} \leftarrow: MoO_4^{2-}$) result in the precipitation of $(Ba,Sr)MoO_4$ crystals:

$$Ba(NO_3)_{2(s)} \rightarrow Ba^{2+}_{(aq)} + 2NO^{-}_{3(aq)} \quad (1)$$

$$Sr(NO_3)_{2(s)} \rightarrow Sr^{2+}_{(aq)} + 2NO^{-}_{3(aq)} \quad (2)$$

$$Na_2MoO_4\cdot 2H_2O_{(s)} \rightarrow 2Na^{+}_{(aq)} + MoO^{2-}_{4(aq)} + 2H_2O \quad (3)$$

$$Ba^{2+}_{(aq)} + 2NO^{-}_{3(aq)} + Sr^{2+}_{(aq)} + 2NO^{-}_{3(aq)} + 2Na^{+}_{(aq)} + MoO^{2-}_{4(aq)} + 2H_2O \rightarrow (Ba,Sr)MoO_{4(s)} + 2Na^{+}_{(aq)} + 4NO^{-}_{3(aq)} + 2H_2O \quad (4)$$

After precipitation, the resulting suspensions were washed with deionized water several times. Finally, the white precipitates were collected and dried in a conventional furnace at 323 K for 8 h.

Other methods of addition of the ion precursors for the co-precipitation synthesis of $(Ba_{1-x}Sr_x)MoO_4$ crystals were realized. However, we have observed the formation of an additional phase. Tests were also made with other flow rates of drip for the co-precipitation methods, and again the formation of an additional phase was observed. Thus the method of co-precipitation (drop-by-drop) with a flow of 10 ml min^{-1} was found to be extremely effective in the synthesis of monophasic $(Ba_{1-x}Sr_x)MoO_4$ solid solutions.

2.2. Characterizations

$(Ba_{1-x}Sr_x)MoO_4$ crystals, with x = 0, 0.25, 0.50, 0.75 and 1, were characterized by X-ray diffraction (XRD) using a DMax/2500 PC diffractometer (Rigaku, Japan) with Cu $K\alpha$ radiation (λ = 1.5406 Å), at room temperature, in the 2θ range from 20 to 60° with a step size of 0.02° min^{-1}. Rietveld refinements of the measured XRD patterns in the 2θ range from 10 to 110° with a scanning rate of 0.02° min^{-1} were carried out using the general structure analysis (*GSAS*) program (Larson & Von Dreele, 2004). Fourier transform (FT)–Raman spectroscopy was carried out on a Bruker-RFS 100 (Germany) spectrometer. Raman spectra were obtained using the 1064 nm line of an Nd:YAG laser; its maximum output power was maintained at 100 mW in the range from 50 to 1100 cm^{-1}. FT–IR spectra were recorded in the range from 200 to 1000 cm^{-1} using KBr pellets as a reference in a Bomem–Michelson (model MB-102) spectrophotometer in the transmittance mode. The shapes and sizes of these $(Ba_{1-x}Sr_x)MoO_4$ crystals were observed with a field-emission scanning electron microscope model Inspect F50 (FEI Company, Hillsboro, USA) operated at 15 kV. UV–Vis spectra were taken using a Cary 5G spectrophotometer (Varian, USA) in diffuse reflection mode. PL measurements were made with a Monospec 27 monochromator (Thermal Jarrel Ash, USA) coupled to an R446 photomultiplier (Hamamatsu Photonics, Japan). A krypton ion laser (Coherent Innova 90K, USA) (λ = 350 nm) was used as the excitation source; its maximum output power was maintained at 500 mW. After passing through an optical chopper, the maximum laser power was reduced and maintained at 40 mW

Table 1
Lattice parameters, unit-cell volume, site occupancy and statistical parameters of quality obtained by Rietveld refinement for the $(Ba_{1-x}Sr_x)MoO_4$ crystals (with x = 0, 0.25, 0.50, 0.75 and 1) synthesized at 343 K by the co-precipitation method.

	Lattice parameters							
Refined formula $(Ba_{1-x}Sr_xMoO_4)$	a, b (Å)	c (Å)	Cell volume (Å^3)	Occupancy	R_{Bragg} (%)	χ^2 (%)	R_{wp} (%)	R_p (%)
x = 0	5.584828 (21)	12.82922 (9)	400.147 (4)	$BaMoO_4$	4.18	2.759	9.20	6.56
x = 0.25	5.54906 (5)	12.66803 (22)	390.074 (10)	$(Ba_{0.727}Sr_{0.273})MoO_4$	3.42	3.333	8.98	6.58
x = 0.50	5.50729 (9)	12.4789 (4)	378.486 (14)	$(Ba_{0.40845}Sr_{0.59155})MoO_4$	3.35	2.974	8.35	6.09
x = 0.75	5.45711 (5)	12.25476 (23)	364.947 (8)	$Ba_{0.19285}Sr_{0.80715}MoO_4$	2.69	3.705	8.59	6.29
x = 1	5.402647 (22)	12.04112 (8)	351.463 (4)	$SrMoO_4$	2.27	2.312	7.01	4.83

on the samples. All experimental measurements were performed at room temperature.

3. Results and discussion

3.1. XRD analyses

Fig. 1 shows typical XRD patterns for the $(Ba_{1-x}Sr_x)MoO_4$ crystals (x = 0, 0.25, 0.50, 0.75 and 1) synthesized at 343 K by the co-precipitation method.

The XRD patterns illustrated in Fig. 1 revealed that all of the diffraction peaks for the $(Ba_{1-x}Sr_x)MoO_4$ crystals are monophasic and can be indexed to the scheelite-type tetragonal structure with a space group of $I4_1/a$, which is in agreement with the respective Inorganic Crystal Structure Database (ICSD) entries No. 50821 (Nassif *et al.*, 1999) for the $BaMoO_4$ phase and No. 173120 (Bernuy-Lopez *et al.*, 1989) for the $SrMoO_4$ phase. The sharp and well defined diffraction peaks indicate a high degree of crystallinity, *i.e.* all precipitated crystals are structurally ordered at long range, proving the effectiveness of the co-precipitation method employed in this work.

Fig. 1 shows a displacement of all of the diffraction peaks to high values of 2θ angles. According to Bragg's law ($\lambda = 2d\sin\theta$), this displacement of 2θ angles occurs when there is a reduction in the unit-cell lattice parameters. Table 1 lists the results obtained by the analysis of the Rietveld refinement (§3.2); the increase in the x content produces a reduction in the lattice parameters of the $(Ba_{1-x}Sr_x)MoO_4$ crystals. This behavior is due to the replacement of $[BaO_8]$ clusters by $[SrO_8]$ clusters, since $[SrO_8]$ clusters have a minor electronic density in relation to $[BaO_8]$ clusters.

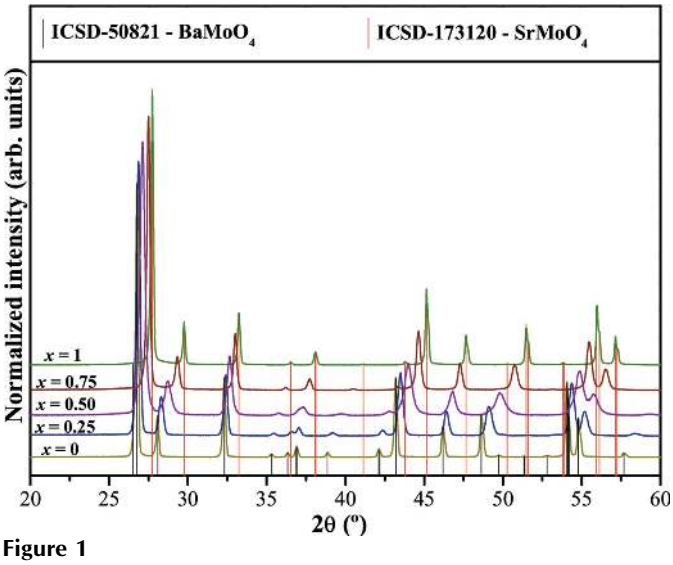

Figure 1
XRD patterns for the $(Ba_{1-x}Sr_x)MoO_4$ crystals (x = 0, 0.25, 0.50, 0.75 and 1). The vertical lines indicate the positions and intensities of the peaks for ICSD card No. 50821 for the $BaMoO_4$ phase and card No. 173120 for the $SrMoO_4$ phase.

3.2. Rietveld refinements analyses

The Rietveld method is based on the construction of diffraction patterns calculated according to a structural model (Rietveld, 1969). The patterns calculated with a fit of the adjustment in relation to observed pattern data provide the structural parameters of the material and the diffraction profile. In this work, the Rietveld method was applied to adjust cell and other parameters, such as lattice parameters, atomic positions and occupancy.

In these analyses, the refined parameters were the scale factor, background, shift lattice constants, profile half-width parameters (u, v, w), isotropic displacement parameters, lattice parameters, strain anisotropy factor, preferred orientation, occupancy and atomic functional positions. The background was corrected using a Chebyschev polynomial of the first kind. A peak profile function was modeled using a convolution of the Thompson–Cox–Hastings pseudo-Voigt (pV–TCH) (Thompson *et al.*, 1987) function with the asymmetry function described by Finger *et al.* (1994), which accounts for the asymmetry owing to axial divergence. To account for the anisotropy in the half-width of the reflections, the model by Stephens (1999) was used.

Figs. 2(*a*)–2(*e*) show the Rietveld refinement plots for the observed patterns *versus* the calculated patterns of $(Ba_{1-x}Sr_x)MoO_4$ crystals (x = 0, 0.25, 0.50, 0.75 and 1).

The measured diffraction patterns are well adjusted to the ICSD entries No. 50821 (Nassif *et al.*, 1999) and No. 173120 (Bernuy-Lopez *et al.*, 1989). However, the region of lower angles where the most intense peaks are located reveals a major difference. The increase in the difference in this region can be related to characteristics of the patterns, with narrow peaks and high intensity. Moreover, $(Ba_{1-x}Sr_x)MoO_4$ crystals have a low density which can influence the collection of data points. In general, however, the differences between the XRD pattern profiles observed experimentally and the theoretically

Table 2
Atomic coordinates (x, y, z) obtained by Rietveld refinement for the $(Ba_{1-x}Sr_x)MoO_4$ crystals (x = 0, 0.25, 0.50, 0.75 and 1) synthesized at 343 K by the co-precipitation method.

	$(Ba_{1-x}Sr_x)MoO_4$				
Atoms	x = 0	x = 0.25	x = 0.50	x = 0.75	x = 1
Ba	0, 0.25, 0.625	0, 0.25, 0.625	0, 0.25, 0.625	0, 0.25, 0.625	–
Mo	0, 0.25, 0.125	0, 0.25, 0.125	0, 0.25, 0.125	0, 0.25, 0.125	0, 0.25, 0.125
O	0.22831, 0.13536, 0.04996	0.23451, 0.12889, 0.0489	0.22856, 0.12659, 0.05165	0.24695, 0.12065, 0.04611	0.2318, 0.11359, 0.0463
Sr	–	0, 0.25, 0.625	0, 0.25, 0.625	0, 0.25, 0.625	0, 0.25, 0.625

calculated data are near to zero in the intensity scale, as illustrated by the line $Y_{obs} - Y_{calc}$. More details regarding the Rietveld refinements are given in Table 1.

This table shows low deviations of the statistical parameters R_{wp}, R_p, R_{Bragg} and χ^2, which indicate the good quality of the structural refinements and the numerical results. Structural refinement data confirm that all $(Ba_{1-x}Sr_x)MoO_4$ crystals are crystallized in a scheelite-type tetragonal structure with the Hermann–Mauguin symmetry space group $I4_1/a$ and four molecular formula units per unit cell (Z = 4) (Panchal *et al.*, 2006; Bi *et al.*, 2009; Cavalcante *et al.*, 2013). However, some variations in the atomic positions related to oxygen atoms were observed, while the barium, strontium and molybdenum atoms have fixed atomic positions (Table 2). These results indicate that the positions of the oxygen atoms are very variable in the lattice as shown by the X-ray powder diffraction data technique. Therefore, we believe these variations in the atomic positions of the oxygen atoms can lead to the formation of different types of distortion of the Ba—O, Sr—O and/or Mo—O bonds and consequently produce different levels of distortion of the deltahedral $[BaO_8]/[SrO_8]$ clusters and/or tetrahedral $[MoO_4]$ clusters in the lattice (Cavalcante, Longo *et al.*, 2012).

3.3. Lattice parameters and unit-cell volume analyses

Figs. 3(*a*) and 3(*b*) illustrate the lattice parameters and the unit-cell volume of the $(Ba_{1-x}Sr_x)MoO_4$ crystals (x = 0, 0.25, 0.50, 0.75 and 1).

Fig. 3(*a*) shows a reduction in the lattice-parameter values with the substitution of strontium for barium atoms. According to the literature (Rosa *et al.*, 2008; Marques *et al.*, 2008), the ionic radius of Ba^{2+} (0.149 nm) is greater than that of Sr^{2+} (0.132 nm). Our results and interpretations employing structural refinement indicated that the reduction in the lattice-parameter values is due to the replacement of deltahedral $[BaO_8]$ clusters by deltahedral $[SrO_8]$ clusters, which cause a reduction in the electron density in the A site of the

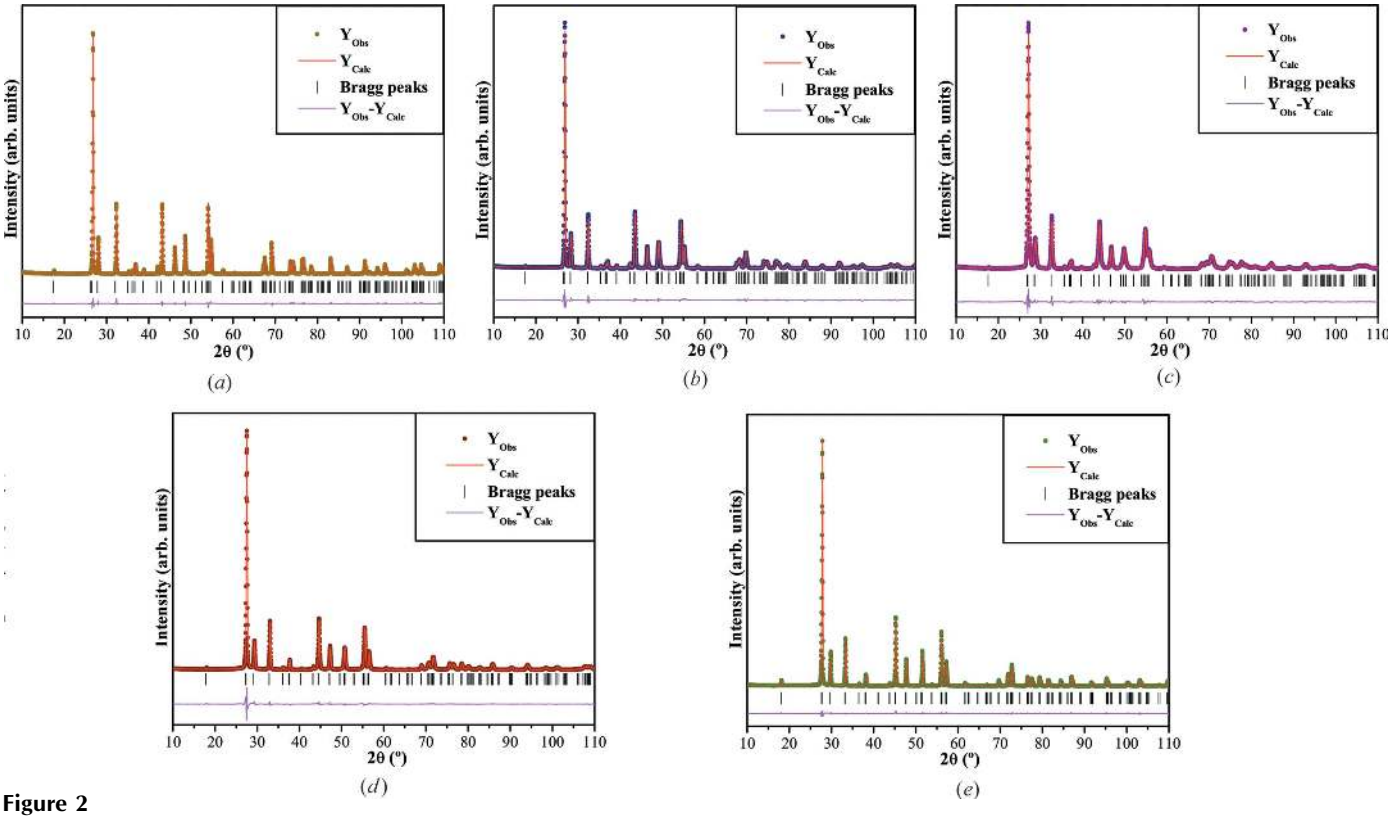

Figure 2
Rietveld refinements of the $(Ba_{1-x}Sr_x)MoO_4$ crystals: (*a*) x = 0, (*b*) x = 0.25, (*c*) x = 0.50, (*d*) x = 0.75 and (*e*) x = 1.

scheelite-type tetragonal structure (Xia *et al.*, 2001). Moreover, we have also verified that contraction in the unit-cell volume [see Fig. 3(*a*) and inset] owing to the increase in the *x* content in the $(Ba_{1-x}Sr_x)MoO_4$ crystals can be related to a possible reduction in the electronic density in the lattice promoted by the deltahedral $[SrO_8]$ clusters. This behavior is related to the radial nature of the chemical bonds and higher electron density of the deltahedral $[BaO_8]$ clusters.

3.4. Representation of the $(Ba_{1-x}Sr_x)MoO_4$ unit cells

Figs. 4(*a*)–4(*e*) show a schematic representation of the unit cells for $(Ba_{1-x}Sr_x)MoO_4$ crystals ($x = 0$, 0.25, 0.50, 0.75 and 1).

These unit cells were modeled with *Diamond* (Brandenburg & Putz, 2011), a crystal and molecular structure visualization program, using lattice parameters and atom positions obtained from the Rietveld refinement data from Tables 1 and 2. All $(Ba_{1-x}Sr_x)MoO_4$ crystal compositions belong to a scheelite-type tetragonal structure with space group $I4_1/a$, point-group symmetry C_{4h}^6 and four molecular formula units per unit cell ($Z = 4$) (Panchal *et al.*, 2006; Cavalcante *et al.*, 2013). Figs. 4(*a*)–4(*e*) show that bonds between O—Mo—O, O—Ba—O and O—Sr—O atoms are projected out of the unit cells. In all of these unit cells, molybdenum atoms are coordinated to four oxygen atoms which form tetrahedral $[MoO_4]$ clusters with a symmetry group T_d and tetrahedron polyhedra (four vertices, four faces and six edges). These tetrahedral $[MoO_4]$ clusters are slightly distorted in each of the $(Ba_{1-x}Sr_x)MoO_4$ crystal lattices. Moreover, these molecular distortions in the $[MoO_4]$ clusters cause changes in the O—Mo—O angles which can produce different levels of structural order–disorder in crystal lattices with $x = 0$, 0.25, 0.50, 0.75 and 1. In addition, for all unit cells, barium and strontium atoms are bonded to eight oxygen atoms, which results in deltahedral $[BaO_8]$/$[SrO_8]$ clusters with a symmetry group of D_{2d} and snub disphenoid polyhedra (eight vertices, 12 faces and 18 edges). Therefore, the deltahedral $[SrO_8]$ clusters have the same coordination as the deltahedral $[BaO_8]$ clusters in the *A* site and different electronic densities. Figs. 4(*a*)–4(*e*) show a model based on Rietveld refinement data for $(Ba_{1-x}Sr_x)MoO_4$ crystals obtained at 343 K by the co-precipitation method. This synthesis method is more effective for the replacement of Ba atoms by Sr atoms in the $BaMoO_4$ crystal lattice, which at short range becomes a local homogeneous arrangement of deltahedral $[BaO_8]$/$[SrO_8]$ clusters in the *A* site of the tetragonal lattice. Moreover, FT–Raman spectroscopy verifies that these deltahedral $[SrO_8]$–$[BaO_8]$–$[SrO_8]$ clusters are well distributed in the lattice and thereby form a homogeneous solid solution, as discussed in the following section.

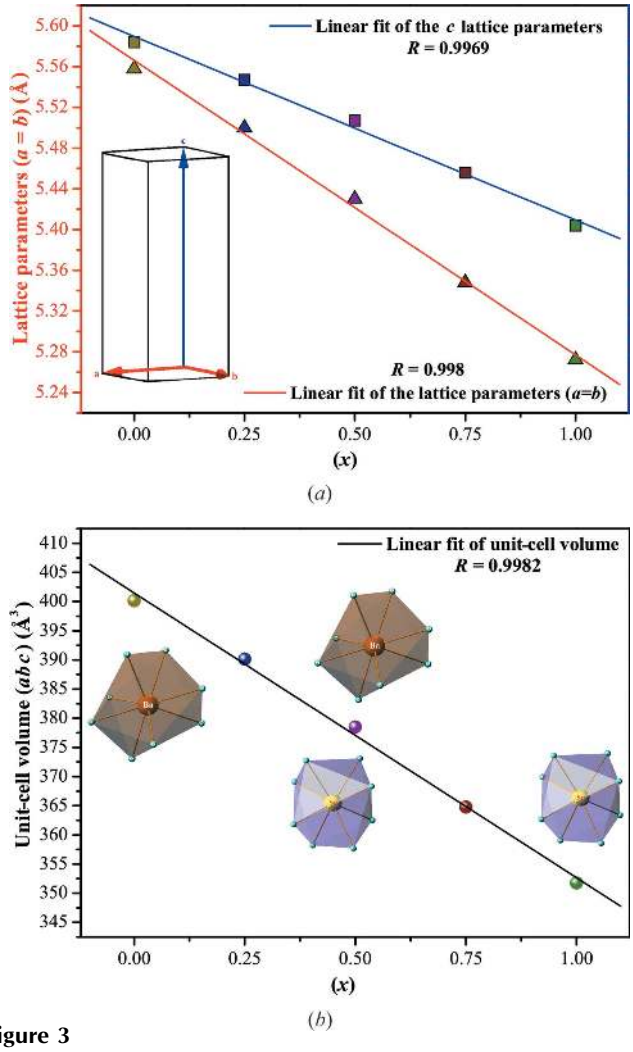

Figure 3
(*a*) Lattice parameters and (*b*) unit-cell volume of the $(Ba_{1-x}Sr_x)MoO_4$ crystals ($x = 0$, 0.25, 0.50, 0.75 and 1).

3.5. Fourier transform–Raman and Fourier transform–infrared spectroscopy analyses

In this work, Raman spectroscopy investigations reveal the effect of the replacement of Ba^{2+} by Sr^{2+} ions in the $(Ba_{1-x}Sr_x)MoO_4$ crystal lattice as well as Raman-active vibration modes at short range. According to group theory calculation, molybdates with a scheelite-type tetragonal structure contain 26 different vibration modes (Raman and infrared) (Basiev *et al.*, 2000; Ling *et al.*, 2006) which are represented as follows:

$$\Gamma_{(\text{Raman})+[\text{Infrared}]} = (3A_g + 5B_g + 5E_g) + [5A_u + 3B_u + 5E_u], \quad (5)$$

where A_g, B_g and E_g are Raman-active vibrational modes. The *A* and *B* modes are non-degenerate, while the *E* modes are doubly degenerate. The subscripts g and u indicate the pairs under inversion in centrosymmetric $(Ba_{1-x}Sr_x)MoO_4$ crystals. A_g, B_g and E_g are Raman modes that arise from the same motion of clusters in the $(Ba_{1-x}Sr_x)MoO_4$ crystals. Therefore, 13 Raman-active vibrational modes of the $(Ba_{1-x}Sr_x)MoO_4$ crystals are anticipated (Ling *et al.*, 2006):

$$\Gamma_{\text{Raman}} = 3A_g + 5B_g + 5E_g. \quad (6)$$

According to Basiev *et al.* (2000), vibrational modes observed in Raman spectra for molybdates are classified into two groups (external and internal modes). The external vibration modes are related to lattice phonons which correspond to deltahedral

$[BaO_8]/[SrO_8]$ cluster motion with point symmetry D_{2d} in rigid-cell units. Vibrational internal modes are related to tetrahedral $[MoO_4]$ cluster vibration in the lattice (assuming the center of mass is in a stationary state). Isolated tetrahedral $[MoO_4]$ clusters have a cubic point symmetry (T_d) (Pereira *et al.*, 2012), and their vibrations are composed of four internal modes [$\nu_1(A_1)$, $\nu_2(E)$, $\nu_3(F_2)$ and $\nu_4(F_2)$], one free rotation mode $\nu_{\text{f.r.}}(F_1)$ and one translational mode (F_2). On the other hand, when tetrahedral $[MoO_4]$ clusters are located in the scheelite lattice, their point symmetry is reduced to S_4 (Jia *et al.*, 2010).

In the infrared spectra, we can expect 13 infrared vibrational modes ($5A_u + 3B_u + 5E_u$). However, in vibrational infrared spectra, $1A_u$ and $1E_u$ are acoustic infrared modes, and $3B_u$ are forbidden infrared modes; therefore, these modes are infrared inactive. Thus, only eight infrared-active vibration modes remain, as illustrated by the following equation (Porto & Scott, 1967):

$$\Gamma_{\text{Infrared}} = 4A_u + 4E_u. \quad (7)$$

Fig. 5 shows FT–Raman spectra of $(Ba_{1-x}Sr_x)MoO_4$ (x = 0, 0.25, 0.50, 0.75 and 1) crystals. The relative positions of vibrational Raman-active modes are listed in Table 3.

These spectra represent Raman-active internal modes related to (←O←Mo→O→) symmetric stretching of tetrahedral $[MoO_4]$ clusters assigned as vibration $\nu_1(A_1)$, symmetric bending vibration $\nu_2(E)$, anti-symmetric stretching vibration $\nu_3(F_2)$, anti-symmetric bending vibration $\upsilon_4(F_2)$ and free rotation $\upsilon_{\text{f.r.}}(F_1)$ (Sczancoski *et al.*, 2008). The external modes (υ_{ext}) correspond to the motion of the deltahedral $[BaO_8]/[SrO_8]$ clusters assigned as symmetric bending. Importantly, sharp and intense Raman-active modes suggest a

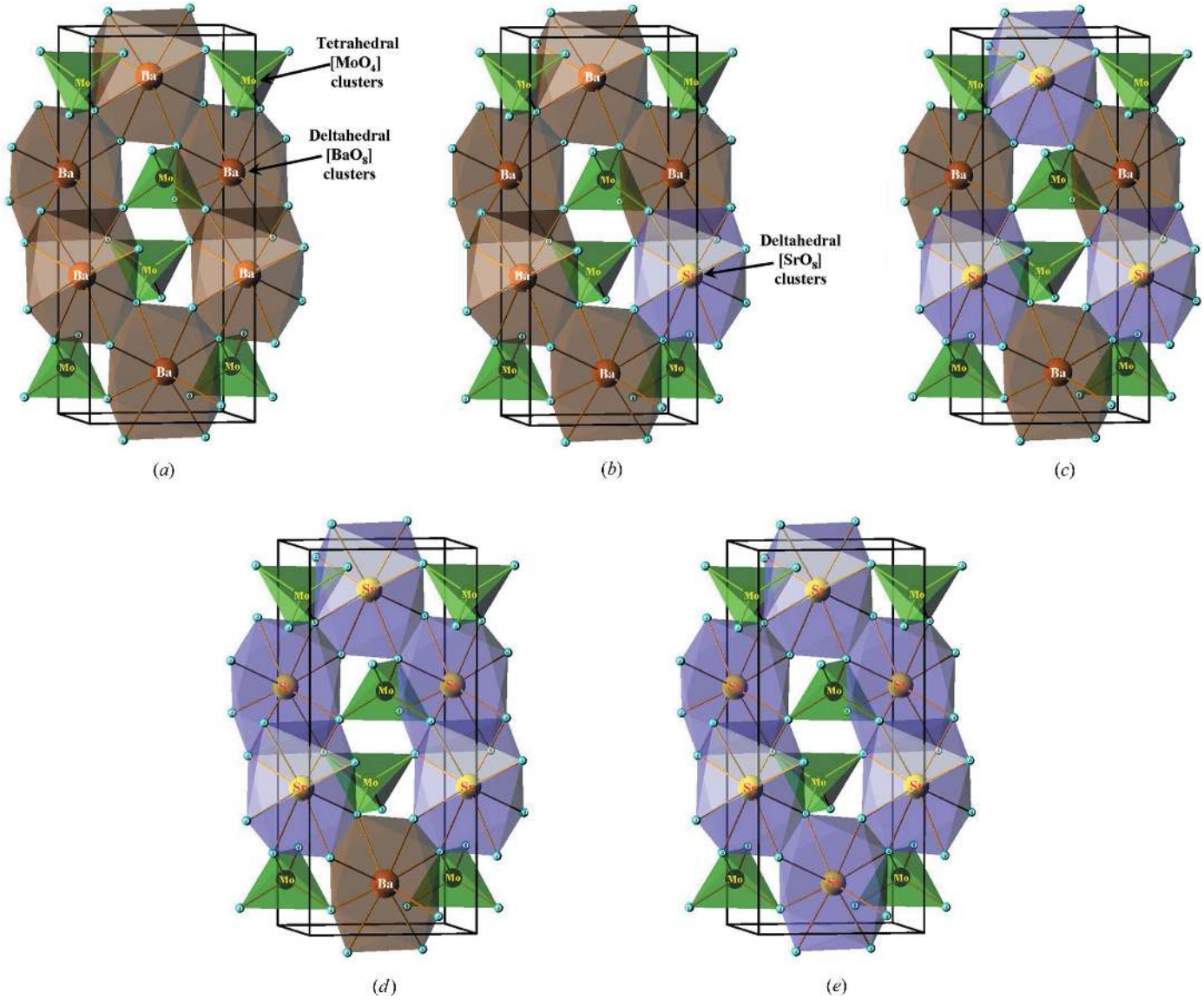

Figure 4
Schematic representation of tetragonal $(Ba_{1-x}Sr_x)MoO_4$ unit cells with $[BaO_8]$–$[SrO_8]$–$[MoO_4]$ clusters. (*a*) x = 0, (*b*) x = 0.25, (*c*) x = 0.50, (*d*) x = 0.75 and (*e*) x = 1.

Table 3
Comparison of results for the experimental Raman-active modes of $(Ba_{1-x}Sr_x)MoO_4$ crystals obtained in this work with those reported in the literature.

Lattice mode symmetry C_{4h}^6	$(Ba_{1-x}Sr_x)MoO_4$ $x = 0$	$x = 0.25$	$x = 0.50$	$x = 0.75$	$x = 1$	$BaMoO_4$ (Marques *et al.*, 2008)	$SrMoO_4$ (Sczancoski *et al.*, 2008)	Assignments
B_g	78	84	86	86	84	76	–	υ_{ext}
E_g	–	–	–	107	97	78	96	
E_g	109	114	122	130	113	107	117	
B_g	140	145	149	155	163	141	137	
A_g			159	170	181		180	$\upsilon_{f.r.}(F_1)$
E_g	190	197	207	222	232	190	–	
A_g	–	–	–	–	–	325	–	$\upsilon_2(E)$
B_g	327	327	327	327	327	326	326	
B_g	346	350	356	361	367	346	383	$\upsilon_4(F_2)$
E_g	360	363	367	375	381	359	387	
E_g	791	791	792	793	795	791	795	$\upsilon_3(F_2)$
B_g	838	840	840	842	845	838	844	
A_g	892	892	892	888	886	891	885	$\upsilon_1(A_1)$

strong interaction between clusters, which arises from the stretching and bending vibrations of the shorter metal–oxygen bonds of deltahedral $[BaO_8]/[SrO_8]$ clusters and tetrahedral $[MoO_4]$ clusters. Therefore, the fact that the Raman-active modes are well defined indicates that the $(Ba_{1-x}Sr_x)MoO_4$ crystals are ordered structurally at short range.

In order to better examine FT–Raman spectra, the regions from 60 to 270, 280 to 420 and 750 to 950 cm^{-1} were amplified (see Figs. SI1–SI3[1]). It is observed that an increase in the concentration of deltahedral $[SrO_8]$ clusters in the $(Ba_{1-x}Sr_x)MoO_4$ crystal lattices produced shift-specific Raman-active modes. The external optical mode shifts to larger vibrational frequencies (Fig. SI1). According to Kanamori *et al.* (1964), in scheelite-type crystals ($AMoO_4$), the A^{2+} cation's mass has a predominant influence on the frequencies of lower external vibrations. This statement is in accordance with the results of FT–Raman spectroscopy. Raman mode frequencies in the $(Ba_{1-x}Sr_x)MoO_4$ crystals increased with a mass reduction of the A^{2+} cation, *i.e.* the substitution of Sr^{2+} for Ba^{2+} cations. This behavior is probably due to lighter metals which interact more strongly with the ionic group $[MoO_4]^{2-}$ and produce higher force constants and increase the vibrational mode frequencies of the $(Ba_{1-x}Sr_x)MoO_4$ crystals. Figs. SI1–SI2 show internal mode frequencies where only the frequency of one $\upsilon_2(E)$ doublet mode is not shifted with the replacement of Ba^{2+} by Sr^{2+} cations; however, other internal mode frequencies [$\upsilon_{f.r.}(F_1)$, $\upsilon_4(F_2)$, $\upsilon_3(B_g)$ and $\upsilon_3(E_g)$] are considerably shifted to larger frequencies. According to data obtained from Rietveld refinement and listed in Table 1, a reduction of the lattice parameters and a contraction of the unit-cell volume with increasing Sr^{2+} concentration is apparent. Consequently, a decrease in the Mo–O distance inside the tetrahedral $[MoO_4]$ clusters increases the force constants for some internal vibrational modes in these groups. The electronegativity of the Ba^{2+} and Sr^{2+} cations is another factor which influences the internal vibrational mode frequency of the $(Ba_{1-x}Sr_x)MoO_4$ lattice. The increased electronegativity of the Sr^{2+} cation results in higher force constants of the stretching vibration in tetrahedral $[MoO_4]$ clusters in Raman vibration modes at higher frequencies. Moreover, the mass of Ba^{2+} and Sr^{2+} cations can also indirectly influence the internal vibration frequencies of tetrahedral $[MoO_4]$ clusters. The formation of Sr—O and Ba—O partially covalent bonds also changes the efficient mass of oscillating atoms of the tetrahedral $[MoO_4]$ clusters. Other factors could be responsible for these phenomena, including differences in the average crystal size, preparation method and degree of structural order–disorder at short range in the lattice.

An opposite situation is observed for the vibrational mode $\upsilon_1(A_1)$ which is related to symmetric stretching of tetrahedral $[MoO_4]$ clusters; the frequency of this vibrational mode is reduced. According to Basiev *et al.* (2000), this phenomenon

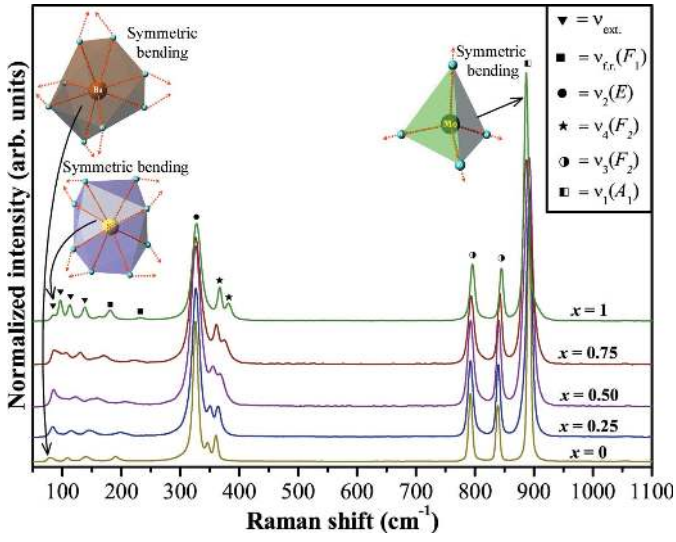

Figure 5
FT–Raman spectra (50–1100 cm^{-1}) of the $(Ba_{1-x}Sr_x)MoO_4$ crystals (x = 0, 0.25, 0.50, 0.75 and 1). The inset shows the symmetric stretching bonds of tetrahedral $[MoO_4]$ clusters and symmetric bending bonds of deltahedral $[BaO_8]/[SrO_8]$ clusters.

[1] The supplementary figures discussed in this paper along with other supplementary data are available from the IUCr electronic archives (Reference: AJ5215). Services for accessing this material are described at the back of the journal.

Table 4
Comparison of results for the experimental infrared-active modes of $(Ba_{1-x}Sr_x)MoO_4$ crystals obtained in this work with those reported in the literature.

Lattice mode symmetry C_{4h}^6	$(Ba_{1-x}Sr_x)MoO_4$ $x = 0$	$x = 0.25$	$x = 0.50$	$x = 0.75$	$x = 1$	$BaMoO_4$ (Sczancoski *et al.*, 2010)	$SrMoO_4$ (Thongtem *et al.*, 2010)	Assignments
E_u	289	287	285	283	276	–	–	$R_{x,y}$
A_u	326	326	326	326	326	–	–	υ_2
E_u/A_u	372	378	388	396	403	439	411	υ_4
E_u	781	783	779	783	788	798	720	υ_3
A_u	825	837	878	876	874	850	970	υ_3

can be explained by Davydov splitting; this effect arises because of strong $[MoO_4]$ molecular group coupling inside a primitive crystal cell.

The displacement of the Raman-active modes as a function of increasing concentration of Sr^{2+} ions can be checked in Table 3.

In this table it is seen that Raman frequencies collected in this work are well correlated with previously published results (Marques *et al.*, 2006; Sczancoski *et al.*, 2008). These results confirm that all of the $(Ba_{1-x}Sr_x)MoO_4$ crystals (x = 0, 0.25, 0.50, 0.75 and 1) synthesized at 343 K by the co-precipitation method have a scheelite-type tetragonal structure at short range.

Fig. 6 shows the FT–IR spectra for the $(Ba_{1-x}Sr_x)MoO_4$ crystals (x = 0, 0.25, 0.50, 0.75 and 1). Vibrational modes of the FT–IR spectra are listed in Table 4.

As discussed in the text above, there are only eight infrared-active vibrational modes for the molybdate crystals with a scheelite-type tetragonal structure (Ling *et al.*, 2006). This work has identified six vibrational modes for $(Ba_{1-x}Sr_x)MoO_4$ crystals (five internal modes and one external mode). Infrared-active internal modes are related to anti-symmetric stretching vibrations in tetrahedral $[MoO_4]$ clusters assigned as $\nu_3[(1E_u)$ and $(1A_u)]$, which correspond to strong absorption bands, anti-symmetric bending vibrations of bonds in tetrahedral $[MoO_4]$ clusters assigned as $\upsilon_4[1(E_u+A_u)]$ and the symmetric bending vibration $\upsilon_2(1A_u)$. $R_{x,y}(1E_u)$ external modes correspond to the torsional motion of tetrahedral $[MoO_4]$ clusters in the lattice. The relative positions for infrared-active modes are shown in Table 4 and are compared with infrared-active modes for crystals prepared by other methods as reported in the literature (Sczancoski *et al.*, 2010; Thongtem *et al.*, 2010).

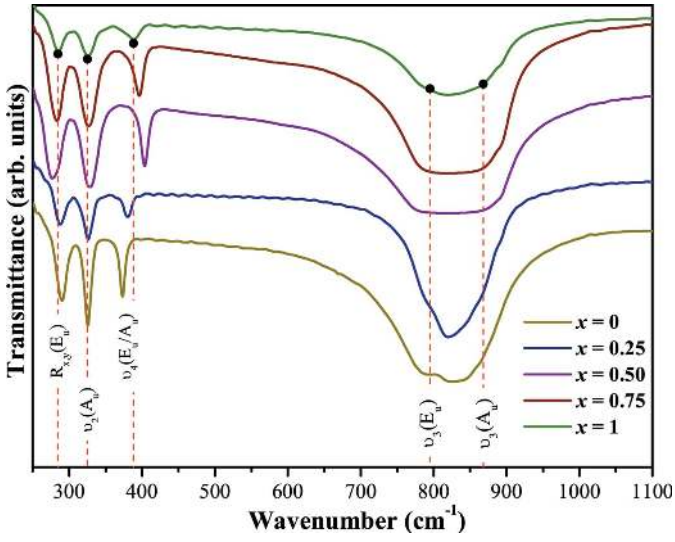

Figure 6
FT–IR spectra (250–1100 cm^{-1}) of the $(Ba_{1-x}Sr_x)MoO_4$ crystals (x = 0, 0.25, 0.50, 0.75 and 1). The vertical lines indicate the positions and relative intensities of infrared-active modes.

According to the data in Table 4, an increase in the concentration of deltahedral $[SrO_8]$ clusters in the $(Ba_{1-x}Sr_x)MoO_4$ crystal lattices produces a shift-specific infrared-active mode; only the frequency of the symmetric bending vibration mode $\upsilon_2(1A_u)$ is not shifted. We believe that vibrational mode frequency shifts can be related to a decrease in the Mo—O bond distance due to the lattice contraction with the replacement of deltahedral $[BaO_8]$ clusters by deltahedral $[SrO_8]$ clusters. This contraction effect is caused by the difference in electron densities and electronegativity between the Ba^{2+} and Sr^{2+} cations and affects the Mo—O bonds in tetrahedral $[MoO_4]$ clusters that are interconnected with $[BaO_4]$–$[MoO_4]$–$[SrO_8]$ neighbors.

3.6. FE-SEM image analyses

Fig. 7 shows FE-SEM images of the $(Ba_{1-x}Sr_x)MoO_4$ crystals (x = 0, 0.25, 0.50, 0.75 and 1).

Fig. 7(*a*) reveals that the $BaMoO_4$ crystals obtained by the co-precipitation method have different sizes and an octahedral shape. This morphological characteristic is particular for scheelite-type $BaMoO_4$ crystals, as has been commonly reported in the recent literature (Mi *et al.*, 2009; Wang *et al.*, 2011; Thirumalai *et al.*, 2012). Fig. 7(*a*) clearly identifies octahedron-like $BaMoO_4$ microcrystals and some nano-octahedrons. The formation of the first $BaMoO_4$ nuclei occurs when the first drop containing a Ba^{2+} ion comes into contact with the solution containing MoO_4^{2-} ions, with subsequent aggregation of several nuclei to form the first small $BaMoO_4$ nanocrystals. After some time, these original nanocrystals grow to form octahedron-like $BaMoO_4$ microcrystals. The last drops of solution containing Ba^{2+} ions that come into contact with the solution containing MoO_4^{2-} ions tend to form smaller $BaMoO_4$ crystals (Kadam *et al.*, 2011; Saleemi *et al.*, 2012). Therefore, in this case, new nucleation events (secondary nucleation) can occur and are characterized by the appearance of small crystals that have not yet grown because they have been formed at the end of the precipitation reaction and lack

further material for growth as employed by the drop-by-drop methodology (see Fig. 7*a*). Fig. 7(*b*) illustrates the influence of Sr^{2+} ion addition in the formation of irregular $(Ba_{0.75}Sr_{0.25})MoO_4$ crystals. According to Wawer *et al.* (2011), in aqueous solution, the Sr^{2+} ions are less solvated than the Ba^{2+} ions; thus a smaller number of water molecules are associated with Sr^{2+} ions in solution, forming a less hydrated sphere of solvation around the central ion. This smaller sphere of hydration facilitates interaction with other ions in the solution, in this case the MoO_4^{2-} anion. This condition is favorable for the increase in the nucleation rate and the heterogeneous secondary nucleation process. Thus, the replacement of Ba^{2+} ions by Sr^{2+} ions retards the growth process of the crystals. This particular characteristic of each salt promotes the nonhomogeneous $(Ba_{0.75}Sr_{0.25})MoO_4$ crystal growth process after these heterogeneous nucleation events. Figs. 7(*c*) and 7(*d*) illustrate a noted major decrease in average crystal sizes with a greater increase in Sr^{2+} ion concentration and the formation of irregular $(Ba_{0.50}Sr_{0.50})MoO_4$ and $(Ba_{0.25}Sr_{0.75})MoO_4$ crystals, respectively. Finally, several $SrMoO_4$ nanocrystals and some large $SrMoO_4$ crystals are visible (see Fig. 7*e*). Clearly, unlike $BaMoO_4$ microcrystals, $SrMoO_4$ tends to form smaller crystals. The $SrMoO_4$ crystal growth is dominated by the self-assembly process between these nanocrystals because of the high surface energies (Liu, Dai *et al.*, 2012).

3.7. UV–Vis absorption spectroscopy and optical band gap analyses

The optical band gap energy (E_{gap}) was calculated by the method proposed by Kubelka & Munk–Aussig (1931). This methodology is based on the transformation of diffuse reflectance measurements to estimate E_{gap} values with good accuracy within the limits of assumptions when modeled in three dimensions (Myrick *et al.*, 2011). It is particularly useful in limited cases of an infinitely thick sample layer. The Kubelka–Munk equation for any wavelength is described as

$$F(R_\infty) = \frac{(1 - R_\infty)^2}{2R_\infty}\frac{k}{s}, \tag{8}$$

where $F(R_\infty)$ is the Kubelka–Munk function or absolute reflectance of the sample. In our case, magnesium oxide (MgO) was the standard sample in reflectance measurements. $R_\infty = R_{sample}/R_{MgO}$ (R_∞ is the reflectance when the sample is infinitely thick), k is the molar absorption coefficient and s is the scattering coefficient. In a parabolic band structure, the optical band gap and absorption coefficient of semiconductor oxides (Smith, 1978) can be calculated by the following equation:

$$\alpha h\nu = C_1(h\nu - E_{gap})^n, \tag{9}$$

where α is the linear absorption coefficient of the material, $h\nu$ is the photon energy, C_1 is a proportionality constant, E_{gap} is the optical band gap and n is a constant associated with the different kinds of electronic transitions (n = 0.5 for a direct allowed, n = 2 for an indirect allowed, n = 1.5 for a direct forbidden and n = 3 for an indirect forbidden). According to Sczancoski *et al.* (2010), $BaMoO_4$ crystals exhibit optical absorption spectra governed by direct allowed electronic transitions between the valence band (VB) and conduction

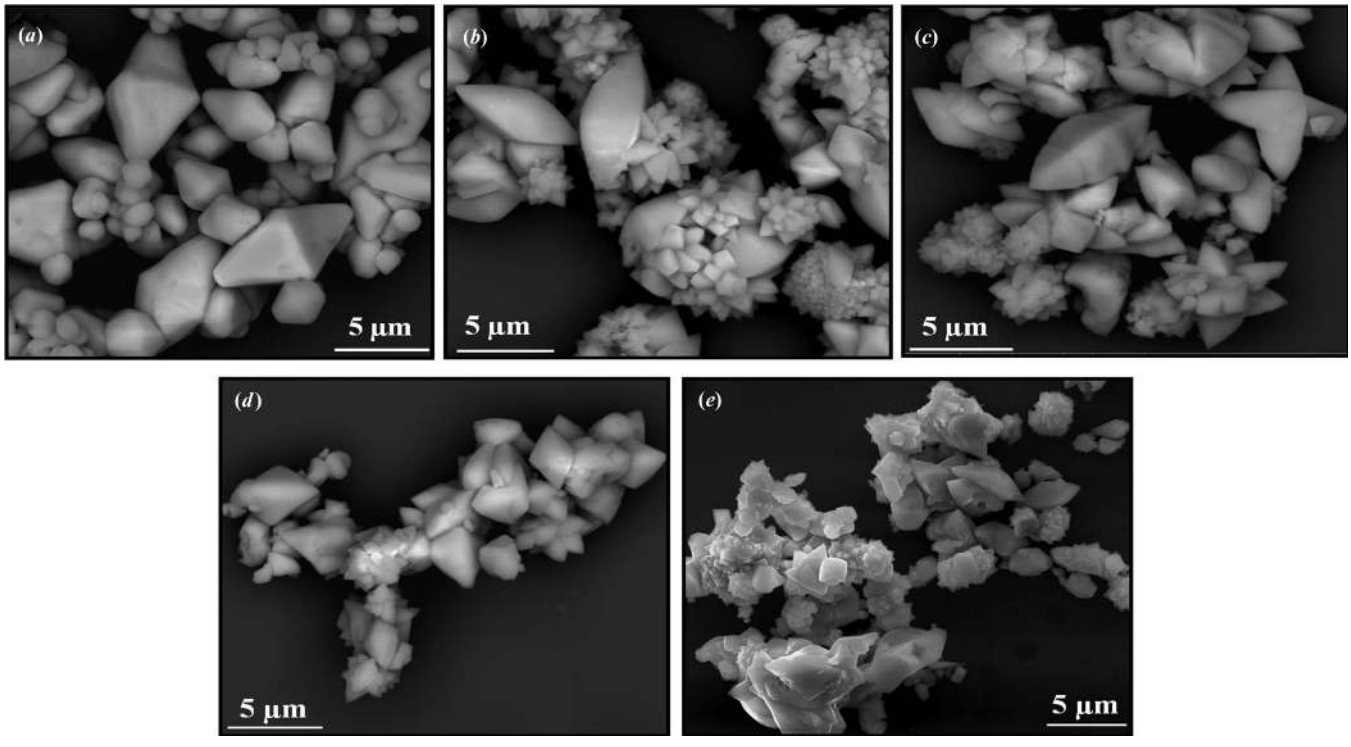

Figure 7
FE-SEM images of the $(Ba_{1-x}Sr_x)MoO_4$ crystals: (*a*) x = 0, (*b*) x = 0.25, (*c*) x = 0.50, (*d*) x = 0.75 and (*e*) x = 1.

band (CB) and exhibited a direct optical band gap of E_{gap} = 4.13 eV. According to Vali (2011), $SrMoO_4$ crystals have a direct optical band gap of E_{gap} = 3.58 eV. This characteristic is observed after the electronic absorption process when electrons located in maximum energy states in the VB go to minimum energy states in the CB at the same point in the Brillouin zone (Sczancoski *et al.*, 2010; Vali, 2011). Therefore, it is proposed in this work that the tetragonal $(Ba_{1-x}Sr_x)MoO_4$ crystals (x = 0, 0.25, 0.50, 0.75 and 1) have E_{gap} experimental results very close to direct allowed transitions. Based on this information, the E_{gap} values of the $(Ba_{1-x}Sr_x)MoO_4$ crystals were calculated using n = 0.5 in equation (9). Finally, using the remission function described in equation (8) and with the term $k = 2\alpha$ and C_2 as a proportionality constant, we obtain the modified Kubelka–Munk equation:

$$[F(R_\infty)h\nu]^2 = C_2(h\nu - E_{gap}). \quad (10)$$

Therefore, finding the $F(R_\infty)$ value from equation (10) and plotting a graph of $[F(R_\infty)h\nu]^2$ against $h\nu$, the E_{gap} values of the $(Ba_{1-x}Sr_x)MoO_4$ crystals were determined.

Figs. 8(*a*)–8(*e*) show the UV–Vis spectra of the $(Ba_{1-x}Sr_x)MoO_4$ crystals (x = 0, 0.25, 0.50, 0.75 and 1), and Fig. 8(*f*) shows optical band gap values as a function of concentration (x).

Figs. 8(*a*)–8(*e*) reveal that the optical band gap for all of the $(Ba_{1-x}Sr_x)MoO_4$ crystals is characterized by well defined direct electronic transitions which are typical of crystalline semiconductor materials with a scheelite-type tetragonal structure (Lacomba-Perales *et al.*, 2008, 2011). The exponential optical absorption edge and the optical band gap energy are controlled by the degree of structural disorder in the lattice. The decrease in the E_{gap} values can be attributed to the increase in local lattice distortions and other localized electronic levels within the forbidden band gap (Longo, Cavalcante *et al.*, 2007). Moreover, it is believed that these differences in E_{gap} (4.25–4.11 eV) values in these crystals are mainly due to different levels of distortion of $[SrO_8]$–$[MoO_4]$–$[BaO_8]$ clusters in the tetragonal lattice at short and medium range. Another interesting factor is the increase in structural distortions due to the replacement of Ba^{2+} by Sr^{2+} ions, which causes a decrease in E_{gap} values.

3.8. PL emission analyses

Fig. 9 shows the PL spectra recorded at room temperature for the $(Ba_{1-x}Sr_x)MoO_4$ crystals, excited by a 350 nm wavelength from a krypton ion laser.

The PL spectra cover a broad band in the range 400–700 nm of the visible electromagnetic spectra, and the profile of the emission band is typical of a multiphonon and multilevel process, *i.e.* a system in which relaxation occurs by several paths involving the participation of numerous states within the band gap of the material (Longo, Orhan *et al.*, 2007). These states are related to the numerous kinds of defects directly associated with the degree of structural order–disorder.

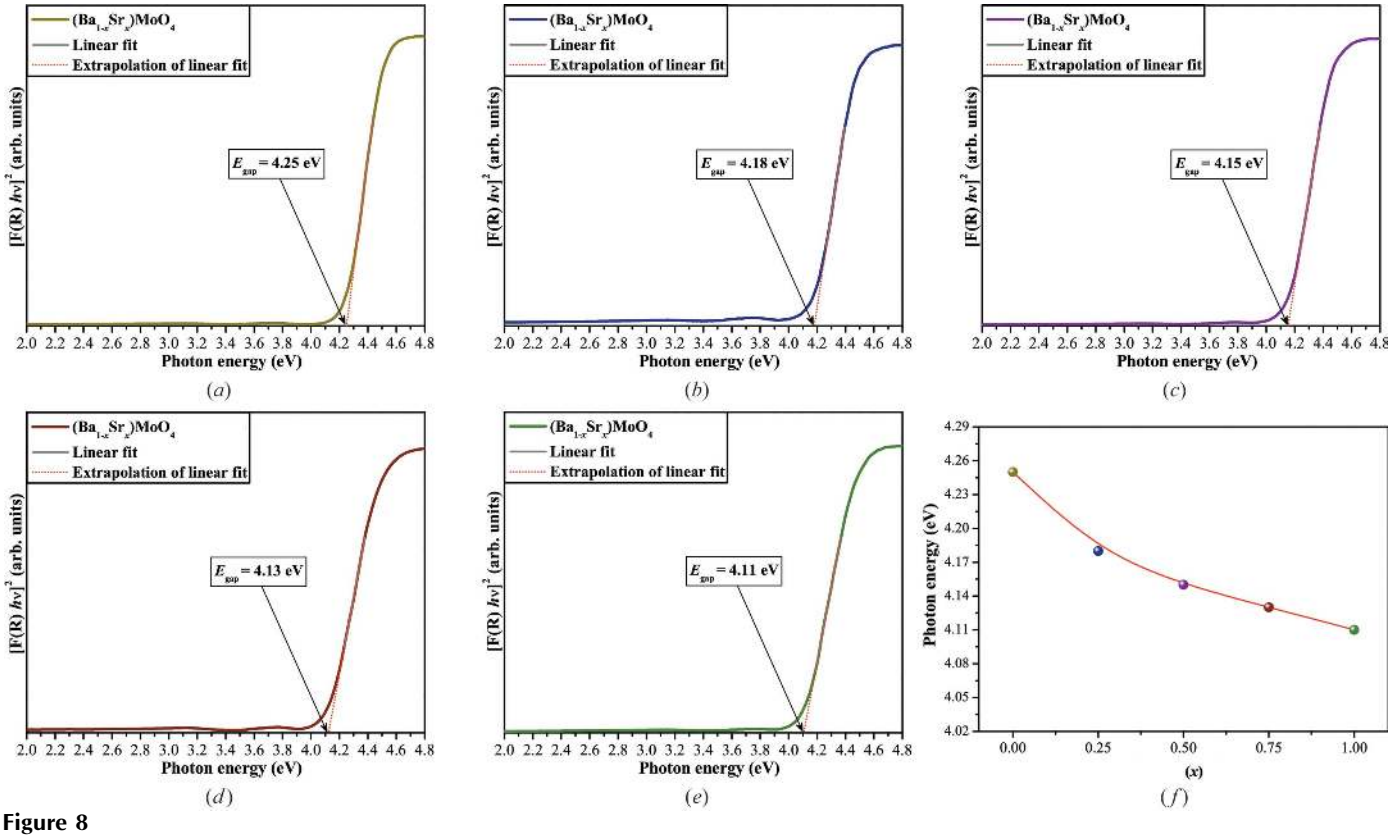

Figure 8
UV–Vis absorbance spectra of the $(Ba_{1-x}Sr_x)MoO_4$ crystals: (*a*) x = 0, (*b*) x = 0.25, (*c*) x = 0.50, (*d*) x = 0.75 and (*e*) x = 1, and (*f*) optical band gap values as a function of the x concentration.

Disorder in materials can be manifested in many ways, *e.g.* vibrational, spin and orientation disorder (all referred to a periodic lattice) and topological disorder. Topological disorder is the type of disorder associated with glassy and amorphous solid structures in which the structure cannot be defined in terms of a periodic lattice. PL is a powerful probe of certain aspects of short-range (2–5 Å) and medium-range (5–20 Å) order for clusters where the degree of local order is such that structurally different sites can be distinguished by modifications in electronic transitions, which are linked to a specific structural arrangement.

As can be seen in Fig. 9, the decrease in the PL of the solid solutions with x = 0.25, 0.50 and 0.75 is due to the disorder promoted by the $[SrO_8]$ clusters. The disorder effect can be related to the increase of defects in the $[BaO_8]$–$[MoO_4]$–$[SrO_8]$ clusters and the presence of intermediary energy levels within the band gap. These results are in agreement with the XRD, FT–Raman spectra and optical band gap measurements.

Several hypotheses have been reported in the literature (Liu *et al.*, 2008; Ryu *et al.*, 2008; Phuruangrat *et al.*, 2009; Ma *et al.*, 2010; Mao *et al.*, 2010; Oh *et al.*, 2010; Thongtem *et al.*, 2010; Sun *et al.*, 2011*b*; Liu, Xia *et al.*, 2012) to explain the possible mechanisms that promote the PL properties and the generation of specific emission colors of $BaMoO_4$ and $SrMoO_4$ crystals. The possible explanations for the improvement of PL properties include control of the morphology/shape, a narrow particle size distribution, the Jahn–Teller splitting effect on the $[MoO_4]^{2-}$ tetrahedron, preferred orientation growth, structural defects, charge transitions within the $[MoO_4]^{2-}$ complexes and surface defects. Regarding the PL properties of $(Ba_{1-x}Sr_x)MoO_4$ solid solutions, Yoshimura *et al.* (1997) have reported an intense PL emission for $(Ba_{0.79}Sr_{0.21})MoO_4$ thin films at cryogenic temperatures.

The theoretical results point out that a symmetry breaking process, associated with order–disorder effects, is a necessary condition for the presence of PL emission. These structural changes can be related to the charge of polarization between distorted clusters that are capable of populating the stable excited electronic states. The central idea to the observation of PL phenomena in $(Ba_{1-x}Sr_x)MoO_4$ crystals is the localization and characterization of excited states that can be considered as trap states implicated in this process. Once these excited states are populated, they may return to lower energy and ground states *via* radiative and/or non-radiative relaxations.

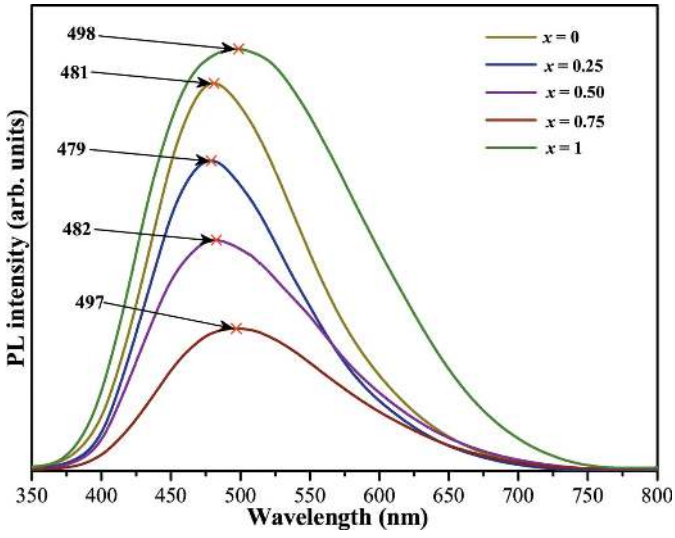

Figure 9
PL emission of the $(Ba_{1-x}Sr_x)MoO_4$ crystals (x = 0, 0.25, 0.50, 0.75 and 1).

Then we can identify three effects in the PL emission of the $(Ba_{1-x}Sr_x)MoO_4$ crystals. The first effect is intrinsic to scheelite material and derived from the bulk material that is constituted by asymmetric distorted tetrahedral $[MoO_4]_d$ clusters and deltahedral $[SrO_8]_d$ and/or $[BaO_8]_d$ clusters (d = disordered). These excited states favor the population of intermediary levels within the band gap of this material and are linked to the universal greenish scheelite luminescence. The second effect is a consequence of the surface defects on the interfaces of complex clusters. The third effect is due to electronic transitions from one cluster to another, which decrease the band gap (E_{gap} = 4.11 eV), allowing a blue PL emission. The interplay between these clusters and defects generates a specific PL emission color.

Based on our findings, we propose an expanded model derived from the wide-band model, to explain the PL behavior. Before arrival of the photon, the short-range $[BaO_8]$, $[SrO_8]$ and $[MoO_4]$ and intermediate-range $[BaO_8]$–$[MoO_4]$ or/and $[SrO_8]$–$[MoO_4]$ structural defects generate localized states within that band gap and a nonhomogeneous charged distribution in the cell. After arrival of the photon, the lattice configuration changes (like a 'breath') and distorted excited clusters are formed, allowing electrons to become trapped. Lastly, the photon decays by radiative or non-radiative relaxations. However, this model represents a paradigm shift toward a better understanding of PL phenomena in scheelite-based materials in general. Although the models presented in this work are limited, they reveal some of the effects of structural order–disorder before and after arrival of the photon that could contribute significantly to PL emissions.

However, the actual factors contributing to the PL behavior of $(Ba_{1-x}Sr_x)MoO_4$ crystals (x = 0.25, 0.50 and 0.75) are still not completely clear. Therefore, a detailed study of the electronic structure of $(Ba_{1-x}Sr_x)MoO_4$ (x = 0.25, 0.50 and 0.75) crystals with *ab initio* calculations to verify the influence of orbitals of Ba and Sr atoms on PL properties of these crystals will be the subject of further research.

4. Conclusions

In summary, we have successfully obtained $(Ba_{1-x}Sr_x)MoO_4$ crystals (x = 0, 0.25, 0.50, 0.75, and 1) at 343 K by the co-precipitation (drop-by-drop) method. XRD patterns and FT–Raman spectra indicate that all $(Ba_{1-x}Sr_x)MoO_4$ crystals are ordered at long and short range with a scheelite-type tetragonal structure without deleterious phases. Rietveld refinement data show that all crystals obtained which form a solid solution were perfect and occurred with a decrease in lattice parameters and unit-cell volume following the increase of x in the lattice. Moreover, these data were employed to model

$[BaO_8]$, $[SrO_8]$ and $[MoO_4]$ clusters by using lattice parameters and atomic positions. Raman-active and IR-active modes reveal typical symmetric/anti-symmetric stretching and bending vibrations of tetrahedral $[MoO_4]$ clusters and deltahedral $[BaO_8]$/$[SrO_8]$ clusters. FE-SEM images show that $(Ba_{1-x}Sr_x)MoO_4$ crystals formed by the co-precipitation (drop-by-drop) method grow from nucleation events (secondary nucleation) that facilitate the growth and appearance of small crystals mixed with large clusters of irregular shape. UV–Vis absorption spectra indicate that the replacement of Ba^{2+} by Sr^{2+} ions produces a decrease in optical band gap values due to the appearance of intermediary energy levels within the band gap. PL spectra presented a broad-band profile typical of a system in which relaxation occurs by several paths involving the participation of numerous states within the band gap of the material. We suggested that these states are related to the defects associated with the asymmetric distorted tetrahedral $[(MoO_4)_d]$ clusters and deltahedral $[(SrO_8)_d$ and $(BaO_8)_d]$ clusters and surface defects on the interfaces of complex clusters. The interplay between these clusters and defects generates a specific PL emission color.

The authors are grateful for the financial support of the Brazilian research financing institutions: CNPq (143505/2009-2, 555684/2009-1, 350711/2012-7), FAPESP-Postdoctorate (No. 2009/50303-4) and CAPES.

References

Afanasiev, P. (2007). *Mater. Lett.* **91**, 4622–4626.

Al-Hajji, L. A., Hasan, M. A. & Zaki, M. I. (2003). *J. Mater. Res.* **18**, 2339–2349.

Azevedo Marques, A. P. de, de Melo, D. M., Paskocimas, C. A., Pizani, P. S., Joya, M. R., Leite, E. R. & Longo, E. (2006). *J. Solid State Chem.* **179**, 671–678.

Basiev, T. T., Sobol, A. A., Voronko, Yu. K. & Zverev, P. G. (2000). *Opt. Mater.* **15**, 205–216.

Bernuy-Lopez, C., Allix, M., Bridges, C. A., Claridge, J. B. & Rosseinsky, M. J. (1989). *Chem. Mater.* **19**, 1035–1043.

Bi, J., Cui, C., Lai, X., Shi, F. & Gao, D. (2008). *Mater. Res. Bull.* **43**, 743–747.

Bi, J., Wu, L., Zhang, Y., Li, Z., Li, J. & Fu, X. (2009). *Appl. Catal. B Environ.* **91**, 135–143.

Bi, J., Xiao, D. Q., Gao, D. J., Yu, P., Yu, G. L., Zhang, W. & Zhu, J. G. (2003). *Cryst. Res. Technol.* **38**, 935–940.

Brandenburg, K. & Putz, H. (2011). *Diamond.* Version 3.2g. University of Bonn, Germany. http://www.crystalimpact.com/diamond.

Cavalcante, L. S., Batista, F. M. C., Almeida, M. A. P., Rabelo, A. C., Nogueira, I. C., Batista, N. C., Varela, J. A., Santos, M. R. M. C., Longo, E. & Siu Li, M. (2012). *RSC Adv.* **2**, 6438.

Cavalcante, L. S., Longo, V. M., Sczancoski, J. C., Almeida, M. A. P., Batista, A. A., Varela, J. A., Orlandi, M. O., Longo, E. & Li, M. S. (2012). *CrystEngComm*, **14**, 853.

Cavalcante, L. S., Sczancoski, J. C., Batista, N. C., Longo, E., Varela, J. A. & Orlandi, M. (2013). *Adv. Powder Technol.* **24**, 344–353.

Cavalcante, L. S., Sczancoski, J. C., Tranquilin, R. L., Joya, M. R., Pizani, P. S., Varela, J. A. & Longo, E. (2008). *J. Phys. Chem. Solids*, **69**, 2674–2680.

Cavalcante, L. S., Sczancoski, J. C., Tranquilin, R. L., Varela, J. A., Longo, E. & Orlandi, M. O. (2009). *Particuology*, **7**, 353–362.

Cui, C., Bi, J., Shi, F., Lai, X. & Gao, D. (2007). *Mater. Lett.* **61**, 4525–4527.

Finger, L. W., Cox, D. E. & Jephcoat, A. P. (1994). *J. Appl. Cryst.* **27**, 892–900.

Guo, X., Zhang, Q., Liu, T., Song, M., Yin, J., Zhang, H. & Wang, X. (2009). *Nucl. Instrum. Methods Phys. Res. Sect. B*, **267**, 1093–1096.

Jia, G., Wang, C. & Xu, S. (2010). *J. Phys. Chem. C*, **114**, 17905–17913.

Kadam, S. S., Kramer, H. J. M. & ter Horst, J. H. (2011). *Cryst. Growth Des.* **11**, 1271–1277.

Kanamori, H., Hayashi, S. & Ikeda, Y. (1964). *J. Phys. Soc. Jpn*, **36**, 511–516.

Kubelka, P. & Munk-Aussig, F. (1931). *Z. Tech. Phys.* **12**, 593–601.

Lacomba-Perales, R., Errandonea, D., Segura, A., Ruiz-Fuertes, J., Rodríguez-Hernández, P., Radescu, S., López-Solano, J., Mujica, A. & Muñoz, A. (2011). *J. Appl. Phys.* **110**, 043703.

Lacomba-Perales, R., Ruiz-Fuertes, J., Errandonea, D., Martínez-García, D. & Segura, A. (2008). *Eur. Phys. Lett.* **83**, 37002.

Larson, A. C. & Von Dreele, R. B. (2004). *General Structure Analysis System (GSAS).* Report LAUR 86-748. Los Alamos National Laboratory, New Mexico, USA.

Lei, F. & Yan, B. (2008). *J. Solid Chem.* **181**, 855–862.

Lei, H., Zhang, S., Zhu, X., Sun, Y. & Fu, Y. (2010). *Mater. Lett.* **64**, 344–346.

Ling, Z. C., Xia, H. R., Ran, D. G., Liu, F. Q., Sun, S. Q., Fan, J. D., Zhang, H. J., Wang, J. Y. & Yu, L. L. (2006). *Chem. Phys. Lett.* **426**, 85–90.

Liu, J., Huang, X., Li, Y. & Li, Z. (2007). *J. Mater. Chem.* **17**, 2754.

Liu, J., Ma, J., Lin, B., Ren, Y., Jiang, X., Tao, J. & Zhu, X. (2008). *Ceram. Int.* **34**, 1557–1560.

Liu, Y. F., Dai, S. H., Lu, Y. N. & Min, H. H. (2012). *Powder Technol.* **221**, 412–418.

Liu, Y. F., Xia, L. L., Lu, Y. N., Dai, S. H., Takeguchi, M., Hong, H. M. & Pan, Z. G. (2012). *J. Colloid Interf. Sci.* **381**, 24–29.

Longo, V. M., Cavalcante, L. S., de Figueiredo, A. T., Santos, L. P. S., Longo, E., Varela, J. A., Sambrano, J. R., Paskocimas, C. A., De Vicente, F. S. & Hernandes, A. C. (2007). *Appl. Phys. Lett.* **90**, 091906.

Longo, V. M., Orhan, E., Cavalcante, L. S., Porto, S. L., Espinosa, J. W. M., Varela, J. A. & Longo, E. (2007). *Chem. Phys.* **334**, 180–188.

Ma, L., Sun, Y., Gao, P., Yin, Y., Qin, Z. & Zhou, B. (2010). *Mater. Lett.* **64**, 1235–1237.

Mao, C. J., Geng, J., Wu, X. C. & Zhu, J. J. (2010). *J. Phys. Chem. C*, **114**, 1982–1988.

Marques, V. S., Cavalcante, L. S., Sczancoski, J. C., Alcântara, A. F. P., Orlandi, M. O., Moraes, E., Longo, E., Varela, J. A., Siu Li, M. & Santos, M. R. M. C. (2010). *Cryst. Growth Des.* **10**, 4752–4768.

Marques, A. P. A., de Melo, D. M. A., Longo, E., Paskocimas, C. A., Pizani, P. S. & Leite, E. R. (2005). *J. Solid State Chem.* **178**, 2346–2353.

Marques, A. P. A., Picon, F. C., Melo, D. M. A., Pizani, P. S., Leite, E. R., Varela, J. A. & Longo, E. (2008). *J. Fluoresc.* **18**, 51–59.

Mi, Y., Huang, Z., Hu, F. & Li, X. (2009). *Mater. Lett.* **63**, 742–744.

Myrick, M. L., Simcock, M. N., Baranowski, M., Brooke, H., Morgan, S. L. & McCutcheon, J. N. (2011). *Appl. Spectrosc. Rev.* **46**, 140–165.

Nassif, V., Carbonio, R. E. & Alonso, J. A. (1999). *J. Solid State Chem.* **146**, 266–270.

Oh, W. C., Park, C. Y., Jeon, J. W. & Lim, C. S. (2010). *Asian J. Chem.* **24**, 2839–2842.

Panchal, V., Garg, N. & Sharma, S. M. (2006). *J. Phys. Condens. Matter*, **18**, 3917–3929.

Pereira, P. F. S., de Moura, A. P., Nogueira, I. C., Lima, M. V. S., Longo, E., de Sousa Filho, P. C., Serra, O. A., Nassar, E. J. & Rosa, I. L. V. (2012). *J. Alloys Compd.* **526**, 11–21.

Phuruangrat, A., Thongtem, T. & Thongtem, S. (2009). *J. Phys. Chem. Solid.* **70**, 955–959.

Porto, S. L., Cassia-Santos, M. R., Santos, I. M. G., Lima, S. J. G., Soledade, L. E. B., Souza, A. G., Paskocimas, C. A. & Longo, E. (2005). *J. Therm. Anal. Calorim.* **79**, 401–406.

Pôrto, S. L., Longo, E., Pizani, P. S., Boschi, T. M., Simões, L. G. P., Lima, S. J. G., Ferreira, J. M., Soledade, L. E. B., Espinoza, J. W. M., Cássia-Santos, M. R., Maurera, M. A. M. A., Paskocimas, C. A., Santos, I. M. G. & Souza, A. G. (2008). *J. Solid State Chem.* **181**, 1876–1881.
Porto, S. P. S. & Scott, J. (1967). *Phys. Rev.* **157**, 716–719.
Pupp, C., Yamdagni, R. & Porter, R. F. (1969). *J. Inorg. Nucl. Chem.* **31**, 2021–2029.
Rangappa, D., Fujiwara, T., Watanabe, T. & Yoshimura, M. (2008). *Mater. Chem. Phys.* **109**, 217–223.
Rietveld, H. M. (1969). *J. Appl. Cryst.* **2**, 65–71.
Rosa, I. L. V., Marques, A. P. A., Tanaka, M. T. S., Melo, D. M. A., Leite, E. R., Longo, E. & Varela, J. A. (2008). *J. Fluoresc.* **18**, 239–245.
Ryu, J. H., Kim, M. M., Park, G. S., Eun, J. W., Shim, K. B. & Lim, C. S. (2008). *Appl. Phys. A*, **92**, 407–412.
Sahu, M., Krishnan, K., Nagar, B. K., Jain, D., Saxena, M. K., Pillai, C. G. S. & Dash, S. (2012). *J. Nucl. Mater.* **427**, 323–332.
Saleemi, A., Rielly, C. & Nagy, Z. K. (2012). *CrystEngComm*, **14**, 2196.
Sczancoski, J. C., Bomio, M. D. R., Cavalcante, L. S., Joya, M. R., Pizani, P. S., Varela, J. A., Longo, E., Siu Li, M. & Andrés, J. A. (2009). *J. Phys. Chem. C*, **113**, 5812–5822.
Sczancoski, J. C., Cavalcante, L. S., Joya, M. R., Varela, J. A., Pizani, P. S. & Longo, E. (2008). *Chem. Eng. J.* **140**, 632–637.
Sczancoski, J. C., Cavalcante, L. S., Marana, N. L., da Silva, R. O., Tranquilin, R. L., Joya, M. R., Pizani, P. S., Varela, J. A., Sambrano, J. R., Siu Li, M., Longo, E. & Andrés, J. (2010). *Curr. Appl. Phys.* **10**, 614–624.
Smith, R. A. (1978). *Semiconductors*, 2nd ed. London: Cambridge University Press.
Spassky, D. A., Ivanov, S. N., Kolobanov, V. N., Mikhailin, V. V., Zemskov, V. N., Zadneprovski, B. I. & Potkin, L. I. (2004). *Rad. Meas.* **38**, 607–610.
Stephens, P. W. (1999). *J. Appl. Cryst.* **32**, 281–289.
Sun, Y., Ma, J., Fang, J., Gao, C. & Liu, Z. (2011*a*). *Ceram. Int.* **37**, 683–686.
Sun, Y., Ma, J., Fang, J., Gao, C. & Liu, Z. (2011*b*). *Inorg. Chem. Commun.* **14**, 1221–1223.
Thirumalai, J., Chandramohan, R., Ahamed, M. B., Ezhilvizhian, S. & Vijayan, T. A. (2012). *J. Mater. Sci. Mater. Electron.* **23**, 325–333.
Thompson, P., Cox, D. E. & Hastings, J. B. (1987). *J. Appl. Cryst.* **20**, 79–83.
Thongtem, T., Kungwankunakorn, S., Kuntalue, B., Phuruangrat, A. & Thongtem, S. (2010). *J. Alloys Compd.* **506**, 475–481.
Thongtem, T., Phuruangrat, A. & Thongtem, S. (2010). *J. Nanopart. Res.* **12**, 2287–2294.
Vali, R. (2011). *Comput. Mater. Sci*, **50**, 2683–2687.
Wang, L. D., Huang, Z. Y., Guo, Y. X. & Wang, T. H. (2011). *Chem. J. Chin. Univ.* **32**, 2838–2843.
Wawer, J., Warmińska, D. & Grzybkowski, W. J. (2011). *Chem. Thermodyn.* **43**, 1731–1737.
Wu, X., Du, J., Li, H., Zhang, M., Xi, B., Fan, H., Zhu, Y. & Qian, Y. (2007). *J. Solid State Chem.* **180**, 3288–3295.
Xia, C. T. & Fuenzalida, V. M. (2003). *J. Eur. Ceram. Soc.* **223**, 519–525.
Xia, C.-T., Fuenzalida, V. M. & Zarate, R. A. (2001). *J. Alloys Compd.* **316**, 250–255.
Yakovyna, V., Zhydachevskii', Y., Mikhailik, V. B., Solskii, I., Sugak, D. & Vakiv, M. (2008). *Opt. Mater.* **30**, 1630–1634.
Yang, P., Li, C., Wang, W., Quan, Z., Gai, S. & Lin, J. (2009). *J. Solid State Chem.* **182**, 2510–2520.
Yin, Y., Gan, Z., Sun, Y., Zhou, B., Zhang, X., Zhang, D. & Gao, P. (2010). *Mater. Lett.* **64**, 789–792.
Yoshimura, M., Ohmura, M., Cho, W. S. & Yashima, M. (1997). *J. Appl. Phys.* **36**, L1229–L1231.
Zhang, C., Shen, E., Wang, E., Kang, Z., Gao, L., Hu, C. & Xu, L. (2006). *Mater. Chem. Phys.* **96**, 240–243.
Zhang, F., Sfeir, M. Y., Misewich, J. A. & Wong, S. S. (2008). *Chem. Mater.* **20**, 5500–5512.